ELSEVIER

Contents lists available at ScienceDirect

### Chemical Engineering Journal

journal homepage: www.elsevier.com/locate/cej





## Luminescent lanthanide single atom composite materials: Tunable full-color single phosphor and applications in white LEDs

Haiyue Yu <sup>a</sup>, Jiancong Liu <sup>a</sup>, Shan Bao <sup>a</sup>, Guoyang Gao <sup>a</sup>, Hongyang Zhu <sup>b</sup>, Peifen Zhu <sup>c,\*</sup>, Guofeng Wang <sup>a,\*</sup>

- <sup>a</sup> Key Laboratory of Functional Inorganic Material Chemistry, Ministry of Education, School of Chemistry and Materials Science, Heilongjiang University, Harbin 150080, PR China
- <sup>b</sup> School of Physics and Electronic Engineering, Linyi University, Linyi 276005, PR China
- <sup>c</sup> Department of Physics and Engineering Physics, The University of Tulsa, Tulsa, OK 74104, USA

#### ARTICLE INFO

# Keywords: Single atom Luminescence Lanthanide CQDs-N MOF LEDs

#### ABSTRACT

Lanthanide single-atom-based CQDs-N:Eu<sup>3+</sup>@MOF-Ln composites were reported for the time. The results of both DFT calculation and experimental characterization show that C atoms can not be replaced by Eu<sup>3+</sup>, but C atoms are more favorable for anchoring Eu<sup>3+</sup> single-atoms. The CQDs modified by N or N/Eu<sup>3+</sup> showed enhanced luminescence intensity. The work function, optical properties, and charge density difference were calculated. The obtained CQDs-N:Eu<sup>3+</sup>@MOF-Ln<sup>3+</sup> composites not only have high thermal stability (up to 510 °C), but also can emit multi-color tunable emissions. Importantly, the white light emission from CQDs-N:Eu<sup>3+</sup>@MOF-Ln<sup>3+</sup> single phosphor with excellent color quality, favorable visual performance, and adjustable color temperature can be obtained by optimizing CQDs-N:Eu<sup>3+</sup>@MOF-Ln<sup>3+</sup>. Not only the WLED devices were constructed with CQDs-N:Eu<sup>3+</sup> and MOF-Ln<sup>3+</sup>, but also the single CQDs-N:Eu<sup>3+</sup>@MOF-Ln<sup>3+</sup> phosphor-based warm WLED devices were realized, and achieves superior color quality (a CRI of 95) and ideal correlated color temperature (a CCT of 4035 K).

#### 1. Introduction

Solid-state white light-emitting diodes (WLEDs) are currently the most prospective lighting technology to take the place of incandescent lamps and fluorescent lamps because of their long life, high luminous efficiency, and energy-saving advantages [1–8]. The current WLEDs are usually manufactured by depositing yellow light-emitting phosphors on blue light-emitting diode chips, but they have a lower color rendering index (CRI) and higher correlated color temperature (CCT) [9,10]. Therefore, further development of new luminescent materials has become the key to overcoming these shortcomings.

Lanthanide doped luminescent materials have been arousing widespread research interest due to their unique optical properties including rich f-orbital configuration, characteristic spectrum, high photochemical stability, and long luminescence lifetimes [11–16]. The potential applications in various fields thus incurred, such as biosensors, cell imaging, drug delivery, and lighting. Among the lanthanide-doped luminescent materials, lanthanide metal—organic frameworks (MOFs-Ln) have become a potential sensor material in chemical sensing because

of their high luminescence quantum yield, high selectivity, and characteristic sharp line emission [17–19]. In particular, MOFs-Ln has attracted great attention in the development of luminescent materials [20–22]. However, the photoluminescence efficiency and stability of MOF-Ln are greatly inhibited because of the non-radiative energy transfer from Ln<sup>3+</sup> to water in MOF-Ln, which results in single-phase bimetallic MOF-Ln phosphors emitting white light with a lower luminous efficacy of radiation (LER) [23]. Therefore, the development of new functional materials is required to obtain higher photoluminescence efficiency and thermal performance. To date, the host—guest approach becomes a novel way to develop advanced multifunctional composite materials [24–26]. A natural habitat is provided by the sustainable pores within MOFs for the guest molecules [27–29].

Fluorescent carbon quantum dots (CQDs) have attracted significant attention as a new type of fluorescent nanomaterials in the past ten years. Compared with other nanoparticles, CQDs have many advantages, including their ultra-fine size, simple synthesis route, high thermal and optical stability, low cost, and environmental friendliness

E-mail addresses: peifen-zhu@utulsa.edu (P. Zhu), 2010070@hlju.edu.cn (G. Wang).

<sup>\*</sup> Corresponding authors.

[30–34]. Despite the superior optical performance of CQDs, some shortcomings need to be overcome for practical applications. Among them, the fluorescence yield of materials prepared by various preparation methods is still low, and it is challenging to adjust and intervene in a targeted manner. Therefore, it is very significant to further improve the optical performance of CQDs. At present, tremendous efforts have been devoted to improving the fluorescence performance of CQDs by optimizing experimental conditions or doping with other elements [35–40].

Metal single atom materials have attracted extensive attention in the scientific research field because of their advantages such as full utilization of atoms, adjustable surface characteristics, special electronic structure, and low cost [41–44]. As far as we know, only six works have been reported on the rare earth single atom materials, including one electrochemical catalysis study and five photocatalysis studies (Supplementary Table 1). However, luminescent materials based on lanthanide single atom have never been reported to date. Reducing lanthanide-doped nanomaterials to a single-atom scale, the unique structural characteristics of lanthanide single atom might give them different or unexpected properties from the nanoscale homologs, which

provides a new opportunity for efficient luminescent materials.

In this study, a novel lanthanide single atom doped composite luminescence materials (CQDs-N:Eu<sup>3+</sup>@MOF-Gd:Eu<sup>3+</sup>/Tb<sup>3+</sup>) with multi-color tunable emission as well as high thermal and light stability are reported. The CQDs-N:Eu<sup>3+</sup> with enhanced luminescence is introduced as a blue fluorescent guest into the MOF-Ln (Ln = Gd, Eu and Tb) host with dual emission centers by a simple one-pot hydrothermal method, forming a novel composite material emitting white light. The density functional theory (DFT) was used to optimize the structures of the CQDs-N:Eu<sup>3+</sup> and MOF-Ln (Ln = Gd, Eu and Tb), and calculate the work function, optical properties, and charge density difference. We can not only construct WLEDs with CQDs-N:Eu<sup>3+</sup> and MOF-Gd:Eu<sup>3+</sup>/Tb<sup>3+</sup> different materials, but also directly construct WLEDs with the CQDs-N: Eu<sup>3+</sup>@MOF-Gd:Eu<sup>3+</sup>/Tb<sup>3+</sup> single composite material. Interestingly, the UV-pumped single CQDs-N:Eu<sup>3+</sup>@MOF-Gd:Eu<sup>3+</sup>/Tb<sup>3+</sup> phosphor-based warm WLED devices with a high CRI of 95 and an ideal CCT of 4035 K were obtained. Our theoretical calculations and experimental results show that the CQDs-N:Eu<sup>3+</sup>@MOF-Gd:Eu<sup>3+</sup>/Tb<sup>3+</sup> obtained in this work has broad application prospects in WLEDs.

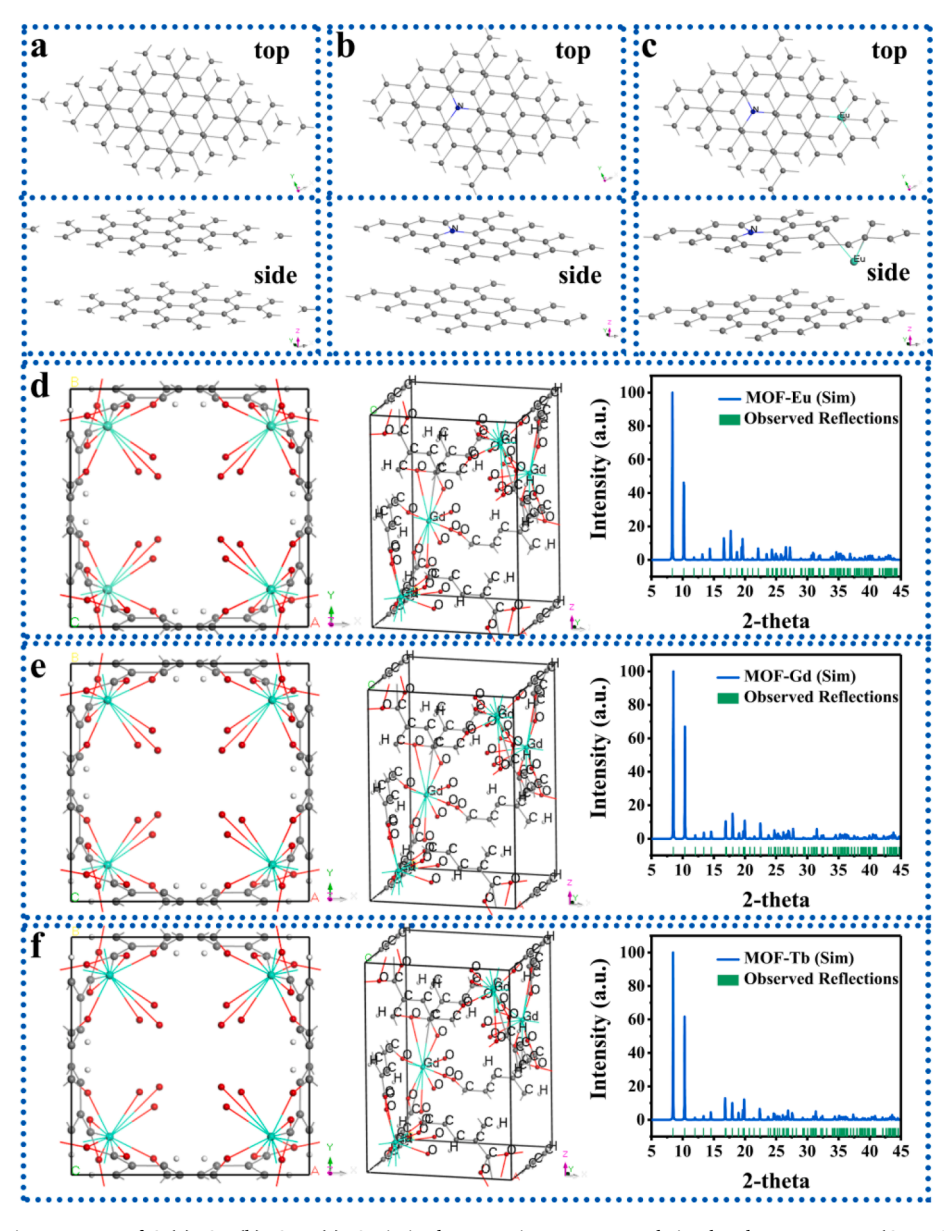


Fig. 1. Optimized geometric structures of C (a), CN (b), CNE (c). Optimized geometric structures and simulated XRD patterns (Cu-K $\alpha$ 1radiation) of MOF-Eu (d), MOF-Gd (e), and MOF-Tb (f).

#### 2. Results and discussion

#### 2.1. Design scheme of overall work

As mentioned above, our goal is to design an efficient fluorescent composite, which has the advantages of CQDs and MOFs-Ln (MOF-76) materials. To obtain a white light single-phase phosphor with high CRI and ideal CCT, the above composites were further doped with different ions at an atomic scale. Specifically, we designed a simple and low-cost hydrothermal synthesis strategy (Supplementary Scheme 1) to obtain the CQDs-N:Ln<sup>3+</sup>@MOF-Ln composites with excellent optical properties. The specific synthesis method is shown in the experimental section. As we expected, the high CRI and ideal CCT were achieved from the single-phase phosphor CQDs-N:Ln<sup>3+</sup>@MOF-Ln by adjusting the content of CQDs-N:Eu<sup>3+</sup>.

#### 2.2. Theory calculation and discussion

The results of DFT calculations indicated that the unique structures are responsible for the unique optical properties. Fig. 1(a, b, c) and Supplementary Fig. 1 show the optimized geometric structures of  $C_{60}$  (C),  $C_{60}N_4$  (CN), and  $C_{54}N_4Eu_4$  (CNE). It is worth noting that  $Eu^{3+}$  replaced the position of C before optimization. However, after optimization,  $Eu^{3+}$  left the original position, resulting in a defect in the (001) surface of C quantum dots. The results indicated that N can easily replace the position of C to form a stable structure, but  $Eu^{3+}$  is difficult to replace C because the radius of  $Eu^{3+}$  is much larger than that of C. Thus, C can not be replaced by  $Eu^{3+}$ , but are more favorable for anchoring as  $Eu^{3+}$  single atoms, which is consistent with previous results [45].

Fig. 1(d, e, f) shows the optimized geometric structures and simulated XRD patterns of MOF-Eu, MOF-Gd, and MOF-Tb. The lattice parameters of MOF-Eu are a=10.61 Å, b=10.61 Å, and c=15.01 Å. The

lattice parameters of MOF-Gd are a=10.47~Å,~b=10.47~Å,~and~c=15.01~Å. The lattice parameters of MOF-Tb are a=10.42~Å,~b=10.42~Å,~and~c=14.96~Å. The variation of lattice parameters is due to the different radii of different rare-earth ions. The shape of the simulated XRD patterns changes only slightly.

Fig. 2 shows the theoretical simulation of optical properties for C, CN, CNE, MOF-Eu, MOF-Tb, and MOF-Gd. The results indicated that the optical properties of C, CN, CNE, MOF-Eu, MOF-Eu, MOF-Tb, and MOF-Gd are different. In particular, the dielectric function is related to the electronic transition and electronic structure in the crystal and can reflect the band structure and optical properties of the materials. The real part of the dielectric function is a measure for the refractive index of a solid, while the imaginary part contains information about the absorption coefficient. These spectral results show that a variety of composite functional materials with different properties can be obtained by adjusting the ratio of CQDs-N:Eu<sup>3+</sup> to MOF-Ln, which can be used in various optoelectronic devices including WLEDs.

Fig. 3a-f shows the calculated Fermi levels, vacuum levels, and work functions of C (001), CN (001), CNE (001), MOF-Eu, MOF-Gd, and MOF-Tb. The abscissa is the fractional coordinates that indicate the position of the crystal lattice input when performing first-principles calculations. The Fermi level increases after N doping. Especially, the Fermi level of CNE is the highest. The increase of the Fermi level indicates the increase of electron concentration. Besides, the values of work functions were 6.098, 4.539, and 3.470 eV for C, CN, and CNE, respectively. The values of work functions were 6.764, 6.363, and 6.023 eV for MOF-Eu, MOF-Gd, and MOF-Tb, respectively.

Fig. 3g-k shows the charge density difference of C, CN, CNE, MOF-Eu, and MOF-Tb. Here, the blue area shows an increase in electron density, whereas the yellow area shows a decrease. All the above theoretical results show that  $\mathrm{Eu}^{3+}$  doping and the combination of CQDs-N: $\mathrm{Eu}^{3+}$  and MOF-Ln are beneficial to the electron transport and the energy transfer

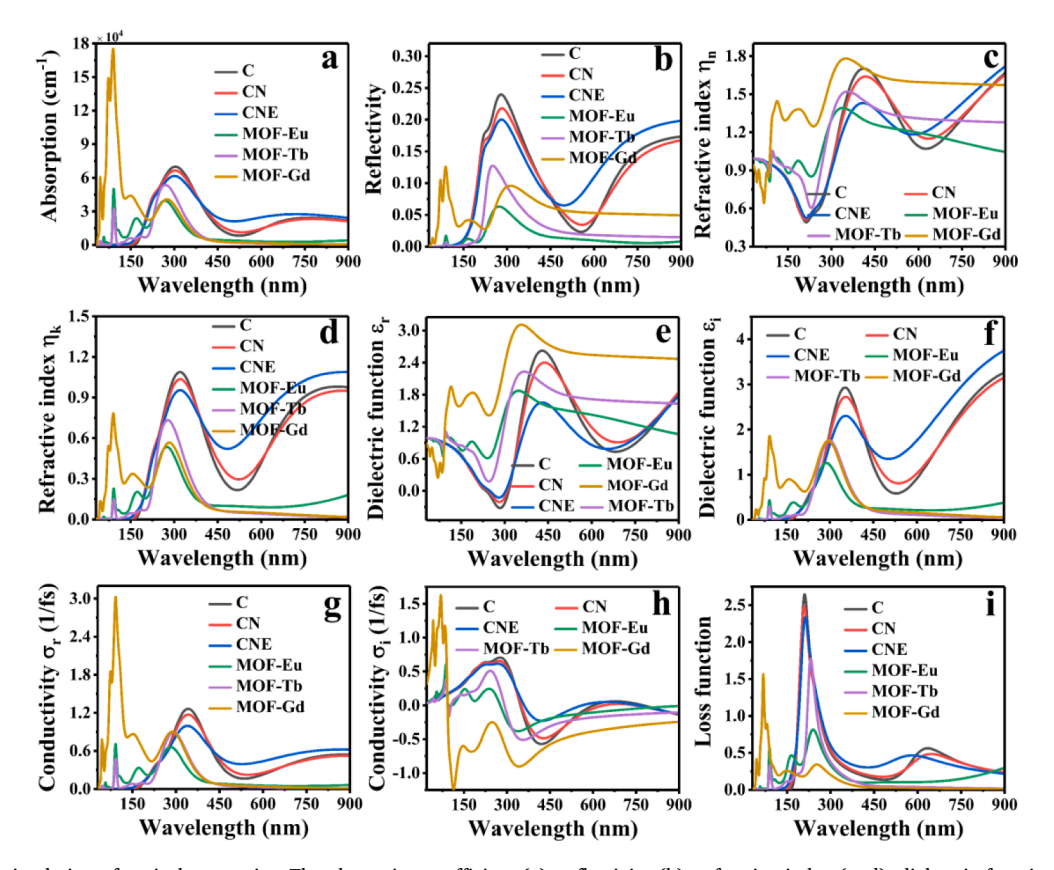


Fig. 2. Theoretical simulation of optical properties. The absorption coefficient (a), reflectivity (b), refractive index (c, d), dielectric function (e, f), optical conductivity (g, h), and loss function (i) of C, CN, CNE, MOF-Eu, MOF-Tb, and MOF-Gd.

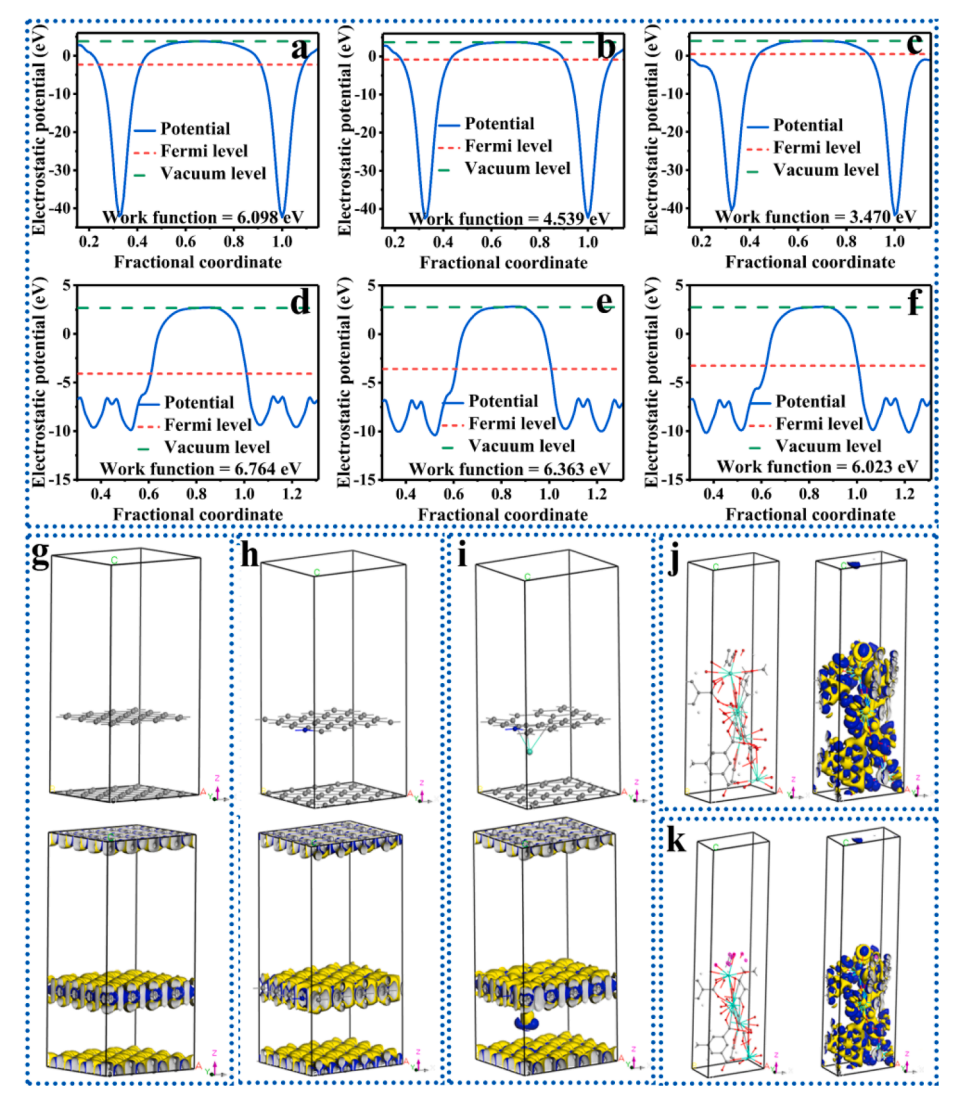


Fig. 3. Calculated Fermi levels, vacuum level, work functions, and charge density difference. Calculated Fermi levels, vacuum levels, and work functions of (a) C, (b) CN, (c) CNE, (d) MOF-Eu, (e) MOF-Gd, and (f) MOF-Tb. Electron density difference of (g) C, (h) CN, (i) CNE, (j) MOF-Eu, and (k) MOF-Tb.

between CQDs-N: $\mathrm{Eu}^{3+}$  and MOF-Ln. This point will be discussed in detail in the spectral discussion section later.

#### 2.3. Structural characterizations

As predicted by our theoretical calculation above, a series of luminescent materials modified by rare earth single atoms were synthesized. The synthesis conditions and sample names are shown in Supplementary Tables 2-5. The scanning electron microscope (SEM), transmission electron microscopy (TEM), and aberration-corrected HAADF-STEM (AC HAADF-STEM) analysis were used to study the morphological characteristics of the samples. The TEM images (Fig. 4a and Supplementary Fig. 2a) of CQDs-N:Eu<sup>3+</sup> reveal the formation of quasi-spherical doped CQDs-N with an average size of 3 nm. Meanwhile, it can be seen from the HRTEM image (Fig. 4b) that the interplanar spacing of the doped CQDs-N is 0.21 nm, which belongs to the (100) plane of graphitic carbon and has high crystallinity. As shown in Supplementary Fig. 2b, c, the SEM images of MOF-Gd:Eu<sup>3+</sup>/Tb<sup>3+</sup> show that it is a large-sized micron rod structure. The STEM image (Fig. 4c) of CNE-5@MOFG shows that the CQDs-N:Eu<sup>3+</sup> is contained in the MOF-Gd:Eu<sup>3+</sup>/Tb<sup>3+</sup> and the excess CQDs-N:Eu<sup>3+</sup> is uniformly attached to the MOF-Gd:Eu<sup>3+</sup>/ Tb<sup>3+</sup> surface. In addition, the SEM images of CNE-5@MOFG and CNE-10@MOFG are shown in Supplementary Fig. 2d-f and it can be

observed that clusters of CQDs-N:Eu $^{3+}$  wrapped on MOF-Gd:Eu $^{3+}$ /Tb $^{3+}$  microrods and the size gradually decreases as the amounts of CQDs-N: Eu $^{3+}$  increases. Surprisingly, the products have a uniform stick shape structure but the size is approximately reduced from about 17  $\mu$ m of pure MOFs to about 2.5  $\mu$ m, which may be due to the incorporation of CQDs-N:Eu $^{3+}$  that restricted the growth of MOF.

To determine the form of the rare-earth ions (Eu<sup>3+</sup>, Gd<sup>3+</sup> and Tb<sup>3+</sup>) in samples, aberration-corrected HAADF-STEM observation was conducted, which shows that the single rare-earth atoms are anchored by C atoms (Fig. 4d-g). In addition, the elemental mapping images of CNE-5@MOFG (Fig. 4h-n) prove that all elements are evenly dispersed in the sample. Although the selected area characterized by the aberration-corrected HAADF-STEM is the location of the CQDs-N:Eu<sup>3+</sup> in CNE-5@MOFG, the elemental mapping images revealed that the CQDs-N:Eu<sup>3+</sup> also contains Gd<sup>3+</sup> and Tb<sup>3+</sup> elements, indicating that Gd<sup>3+</sup> and Tb<sup>3+</sup> ions can be also anchored on the surface of CQDs-N:Eu<sup>3+</sup> during the in-situ synthesis process. Our previous results also showed that the C and N atoms can anchor rare-earth single atom very well [46]. At present, the coordination of a single atom is characterized by synchrotron radiation technology, but the synchrotron radiation test cannot be performed due to the low concentration of rare-earth atoms in our samples.

The X-ray diffraction (XRD) patterns of MOF-Gd:Eu<sup>3+</sup>, MOF-Gd:Eu<sup>3+</sup>/Tb<sup>3+</sup>, CNE-5@MOFG, and CQDs-N:Eu<sup>3+</sup> are shown in

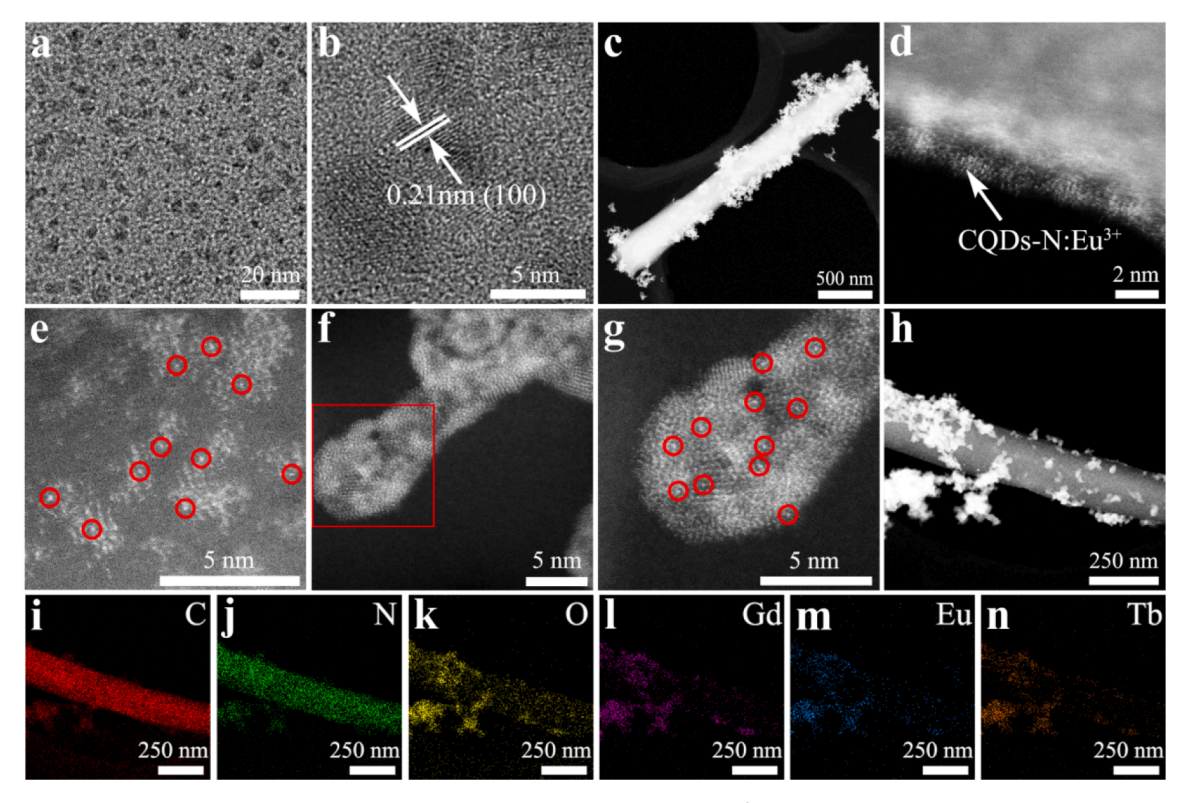
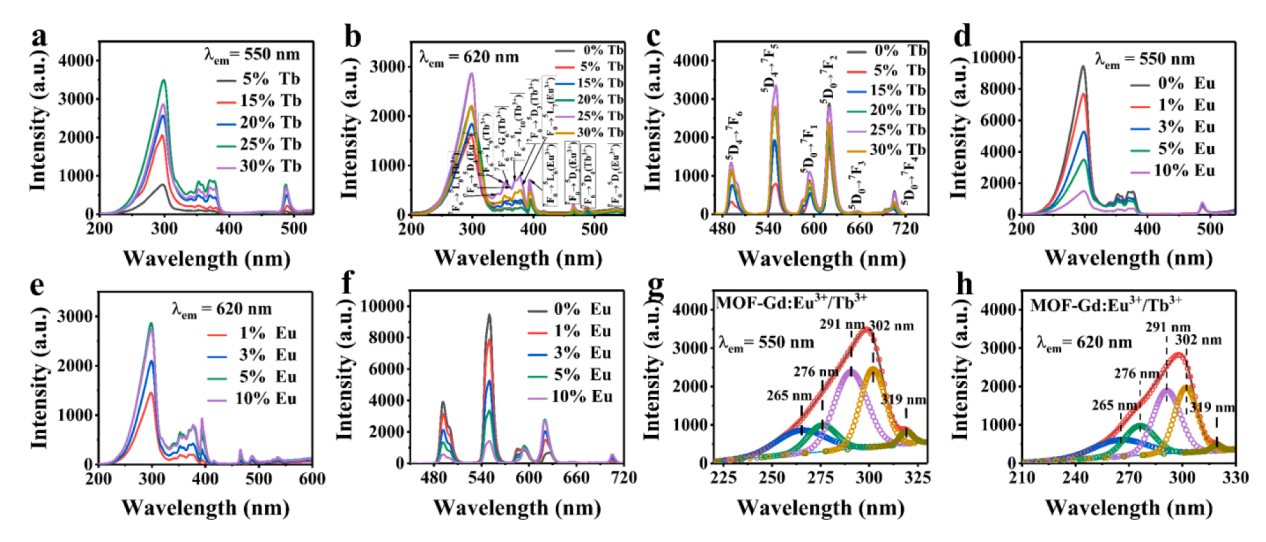


Fig. 4. Morphological characterization of samples. TEM (a) and HR-TEM images (b) of CQDs-N:Eu<sup>3+</sup>. STEM (c, g) images of CNE-5@MOFG. (h, i, j, k, l, m, n) The element mapping images of C, N, O, Gd, Eu, and Tb in CNE-5@MOFG.

Supplementary Fig. 3a. The XRD patterns of MOF-Gd: $Eu^{3+}$  and MOF-Gd: $Eu^{3+}/Tb^{3+}$  were identical with those of the calculated results in Fig. 1d-f, suggesting that the obtained MOF are isostructural with the reported MOF-76 [47]. The XRD pattern of CQDs-N: $Eu^{3+}$  shows a broad (Bragg) reflection (002) centered at around 25 in accordance with the ultrabroad (Bragg) reflection (002) of the graphene structure of the CQDs-N: $Eu^{3+}$ . The broad (Bragg) reflection confirms the graphene structure of the CQDs-N: $Eu^{3+}$ . The XRD pattern of CNE-5@MOFG agrees well with that of the MOF-Gd: $Eu^{3+}$ , and the similar (Bragg) reflections of the MOF-Gd: $Eu^{3+}$  and the CQDs-N: $Eu^{3+}$  fully confirmed that the doping of the CQDs-N: $Eu^{3+}$  does not impact the crystal integrity of MOF-Gd: $Eu^{3+}/Tb^{3+}$ . In addition, the XRD patterns of CNE-x@MOFG (x = 5, 7, 10, and

12) are shown in Supplementary Fig. 3b and it can be observed that the characteristic (Bragg) reflections of MOF-Gd:Eu $^{3+}$ /Tb $^{3+}$  become weaker with the increase of the amount of CQDs-N:Eu $^{3+}$ , which indicates the successful synthesis of the composites.

To further explore the surface structure of CQDs-N:Eu $^{3+}$ @MOF-Gd: Eu $^{3+}$ /Tb $^{3+}$ , we carried out a series of characterizations. Supplementary Fig. 4 shows the Raman spectra of MOF-Gd:Eu $^{3+}$ /Tb $^{3+}$  and the peaks at 1000 and 1500 cm $^{-1}$  are ascribed to the ring respiratory vibration and the vibration of C–H, respectively. The Fourier-transform infrared (FTIR) spectra of CQDs-N:Eu $^{3+}$ , CNE-10@MOFG, CNE-5@MOFG, MOF-Gd:Eu $^{3+}$ /Tb $^{3+}$ , and MOF-Gd:Eu $^{3+}$  are shown in Supplementary Fig. 5 and their characteristic bands are almost the same. See the



**Fig. 5.** Optical performance of MOF-Ln. (a, b, c) Excitation (monitored at 550 and 620 nm) and emission (excited at 297 nm) spectra of MOF-Gd:5%Eu<sup>3+</sup>/x%Tb<sup>3+</sup>. (d, e, f) Excitation (monitored at 550 and 620 nm) and emission (excited at 297 nm) spectra of MOF-Gd:25%Tb<sup>3+</sup>/x%Eu<sup>3+</sup>. (g, h) The excitation bands in the range of 200–330 nm monitored at 550 and 620 nm of MOF-Gd:5%Eu<sup>3+</sup>/25%Tb<sup>3+</sup> can be fitted with five curves.

supplementary information for a detailed discussion.

The UV–vis absorption spectra of MOF-Gd:Eu³+/Tb³+, CQDs-N:Eu³+, and CNE-5@MOFG were analyzed in Supplementary Fig. 6. The absorption peaks of CQDs-N:Eu³+ at 350 nm and 240 nm is attributed to the  $n\to\pi^*$  transitions of C=O and N electronic transitions and  $\pi\to\pi^*$  transitions of the C=C. In addition, CQDs-N:Eu³+ has strong visible-light absorption in the range of 420–700 nm. It is worth noting that when compared with pure MOF, the absorption of the composites in the visible-light region is significantly enhanced and the absorbance is increased, which further proves the successful synthesis of CQDs-N: Eu³+@MOF-Gd:Eu³+/Tb³+ samples.

The Brunauer-Emmett-Teller (BET) surface area of the CNE-5@MOFG is acquired from  $N_2$  adsorption—desorption isotherms (Supplementary Fig. 7). Compared with the pure MOF reported, the BET surface area of the composite is reduced [15], which proves that CQDs-N:Eu³+ can fill the gap or load onto the surface of MOF-Gd:Eu³+/Tb³+. The energy-dispersive X-ray spectroscopy (EDX) analysis on the MOF-Gd:Eu³+/Tb³+ and CNE-5@MOFG composites (Supplementary Fig. 8) indicates that both MOF-Gd:Eu³+/Tb³+ and CNE-5@MOFG consist of C, N, O, Gd, Eu, and Tb. The contents of N and Eu in CNE-5@MOFG are higher than those in MOF-Gd:Eu³+/Tb³+, which proves the successful synthesis of the CQDs-N:Eu³+@MOF-Gd:Eu³+/Tb³+ structures. For more accurate element composition and surface group analyses, the X-ray photoelectron spectroscopy (XPS) spectra of CQDs-N:Eu³+ and CNE-5@MOFG were recorded. See the supplementary information for detailed discussions (Supplementary Figs. 9-11).

Thermogravimetric analysis (TGA) for CNE-5@MOFG and MOF-Gd:  ${\rm Eu}^{3+}/{\rm Tb}^{3+}$  was performed in a flow of N<sub>2</sub>. As shown in Supplementary Fig. 12, the first stage of thermal weight loss of the CNE-5@MOFG composite occurred below 100 °C and plateaued around 150 °C with about 15% weight loss, which is due to the evaporation of the residual solvent. The weight loss of the second stage (from 150 to 510 °C) can be attributed to the initial pyrolysis of ligands in MOF-Gd:Eu<sup>3+</sup>/Tb<sup>3+</sup> and the decomposition of amide groups in CQDs-N:Eu<sup>3+</sup>. The weight loss (about 10%) is lower than that of pure MOF crystal (about 12%), which is due to the presence of CQDs-N:Eu<sup>3+</sup> in the composite materials. During 510–650 °C, the weight loss (from 27 to 47%) represents the collapse of the framework. Consequently, only about 20% weight loss after 510 °C indicates the good thermal stability of CQDs-N:Eu<sup>3+</sup>@MOF-

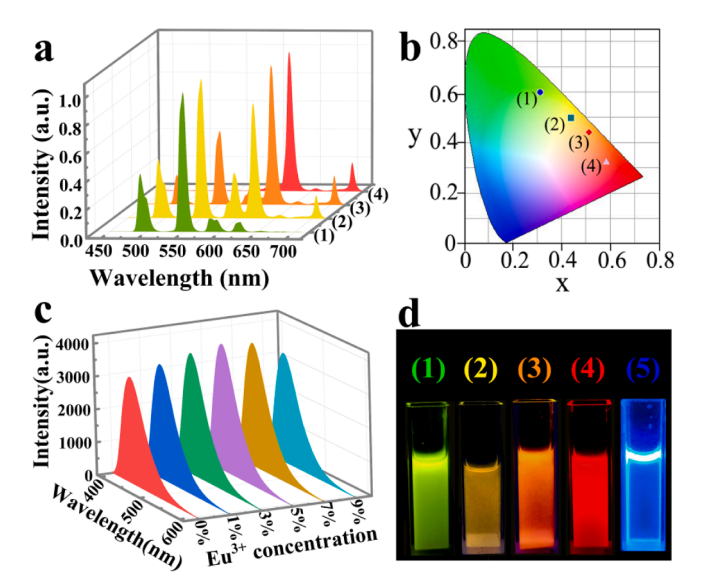


**Fig. 6.** Optical performance and multicolor emission of MOF-Ln and CQDs-N:  $\mathrm{Eu}^{3+}$ . (a,b) Emission spectra and corresponding CIE chromaticity coordinates of MOF-Gd: $\mathrm{Ln}^{3+}$  excited at 297 nm. (c) Emission spectra of the CQDs-N:x% $\mathrm{Eu}^{3+}$  excited at 380 nm. (d) The photographs are the corresponding liquid products under UV light irradiation.

 $Gd:Eu^{3+}/Tb^{3+}$  and MOF- $Gd:Eu^{3+}/Tb^{3+}$ .

#### 2.4. Optical properties

MOF-Gd doped with different Eu<sup>3+</sup> and Tb<sup>3+</sup> concentrations (MOF-Gd:Eu<sup>3+</sup>/Tb<sup>3+</sup>) exhibits down-conversion luminescence characteristics with dual emission centers under the UV light, which is due to the f-f electronic transitions of the Eu<sup>3+</sup> and Tb<sup>3+</sup> in the MOF-Gd matrix. The influent of different Eu<sup>3+</sup> concentrations on the fluorescence properties of MOF-Gd:Eu<sup>3+</sup> was studied. The excitation spectra (Supplementary Fig. 13a) of MOF-Gd:x%Eu<sup>3+</sup> consist of broadband and several sharp excitation peaks. The role of the antenna effect of the organic ligand in MOF-Gd:Eu<sup>3+</sup> and charge transfer band (CTB) Eu<sup>3+</sup> $\rightarrow$  O<sup>2-</sup> lead to the generation of the broad excitation band at 230-330 nm, which leads to the energy transfer to the excitation level of Eu<sup>3+</sup>. In addition, several sharp excitation peaks are ascribed to the characteristic transitions of Eu<sup>3+</sup>. Supplementary Fig. 13b shows the stokes emission spectra of MOF-Gd:Eu<sup>3+</sup> with different Eu<sup>3+</sup> ions concentrations excited at 297 nm. The emission peaks correspond to the transitions of  ${}^5D_0{\rightarrow}^7F_1$  (594 nm),  ${}^5D_0 \rightarrow {}^7F_2$  (620 nm),  ${}^5D_0 \rightarrow {}^7F_3$  (656 nm), and  ${}^5D_0 \rightarrow {}^7F_4$  (705 nm). The intensity of the stokes luminescence increases with the increase of the concentrations of the Eu<sup>3+</sup> ions and starts to decrease when the concentration reaches 5%, which is mainly due to the concentration quenching. The corresponding values of  $\Omega_2$  are shown in Supplementary Table 6. In general, the intensity of the  ${}^5D_0 \rightarrow {}^7F_2$  emission peak is directly affected by the value of  $\Omega_2$ , which is not only related to the local symmetry around Eu<sup>3+</sup> ions, but also affected by the covalency or lowenergetic covalent state or the low energy even state even parity states. Here, the values of  $\Omega_2$  of MOF-Gd:Eu<sup>3+</sup> increase with increasing Eu<sup>3+</sup> concentration.

Fig. 5(a,b) shows the excitation spectra of MOF-Gd:5%Eu<sup>3+</sup>/x%Tb<sup>3+</sup> (x = 0 to 30) monitored at 550 and 620 nm emission. The broadband at 230-330 nm is caused by MOF-Gd matrix absorption and the several sharp excitation peaks are from Eu<sup>3+</sup>/Tb<sup>3+</sup> characteristic transitions. Fig. 5c shows the emission spectra of MOF-Gd:5%Eu $^{3+}$ /x%Tb $^{3+}$  (x = 0 to 30) excited at 297 nm, which shows the  ${}^5D_4 \rightarrow {}^7F_6$  (491 nm) and  $^5D_4 \rightarrow ^7F_5$  (550 nm) transitions of Tb<sup>3+</sup> and the  $^5D_0 \rightarrow ^7F_1$  (594 nm),  $^{5}D_{0} \rightarrow ^{7}F_{2}$  (620 nm),  $^{5}D_{0} \rightarrow ^{7}F_{3}$  (656 nm) and  $^{5}D_{0} \rightarrow ^{7}F_{4}$  (705 nm) transitions of Eu<sup>3+</sup>. Additionally, as Tb<sup>3+</sup> concentration (x) increases, the emission intensity of Tb3+ and Eu3+ increases systematically, which indicates that the energy is transferred from MOF-Gd matrix to  $\mathsf{Tb}^{3+}$  and  ${\rm Eu^{3+}}$  ions. Besides, when  ${\rm Tb^{3+}}$  concentration is low, the energy is mainly transferred from  ${\rm Eu^{3+}}$  to  ${\rm Tb^{3+}}$ , and when  ${\rm Tb^{3+}}$  concentration increases, the energy is mainly transferred to Eu<sup>3+</sup>. The J-O parameters of different samples from emission spectra were calculated (Supplementary Table 7). The values of  $\Omega_2$  of MOF-Gd:5%Eu<sup>3+</sup>/x%Tb<sup>3+</sup> increase with increasing Tb<sup>3+</sup> concentration. The emission peaks of Tb<sup>3+</sup> and Eu<sup>3+</sup> overlap to some extent, which leads to some errors in the calculated J-O parameters. The emission intensity of  ${\rm Tb}^{3+}$  and  ${\rm Eu}^{3+}$  starts to decrease at the same time when the concentration of Tb<sup>3+</sup> reaches 25%, which is mainly due to the concentration quenching.

Similarly, Fig. 5(d,e) shows the spectra of MOF-Gd:5%Tb³+/x%Eu³+ (x = 0 to 10) monitored at 550 and 620-nm emission. Fig. 5f is the emission spectra of MOF-Gd:25%Tb³+/x%Eu³+ (x = 0 to 10). It can be observed from the graph that the emission peak intensity of Tb³+ gradually decreases with increasing Eu³+ concentration, which further indicates that energy is mainly transferred from Tb³+ to Eu³+. Significantly, the characteristic transitions of Tb³+ are found in the excitation spectra of MOF-Gd:25%Tb³+/x%Eu³+ obtained by monitoring at the 620-nm emission, which further proves that energy is transferred from Tb³+ to Eu³+. The values of  $\Omega_2$  of MOF-Gd:25%Tb³+/x%Eu³+ decrease with increasing Eu³+ concentration (Supplementary Table 8). In addition, the excitation bands of MOF-Gd:25%Tb³+/5%Eu³+ by monitoring the 550-nm (Fig. 5g) and 620-nm (Fig. 5h) emission in the range of 230–330 nm were fitted with five curves respectively. These peaks are ascribed to the multiple absorption bands of MOF-Gd ligands and the

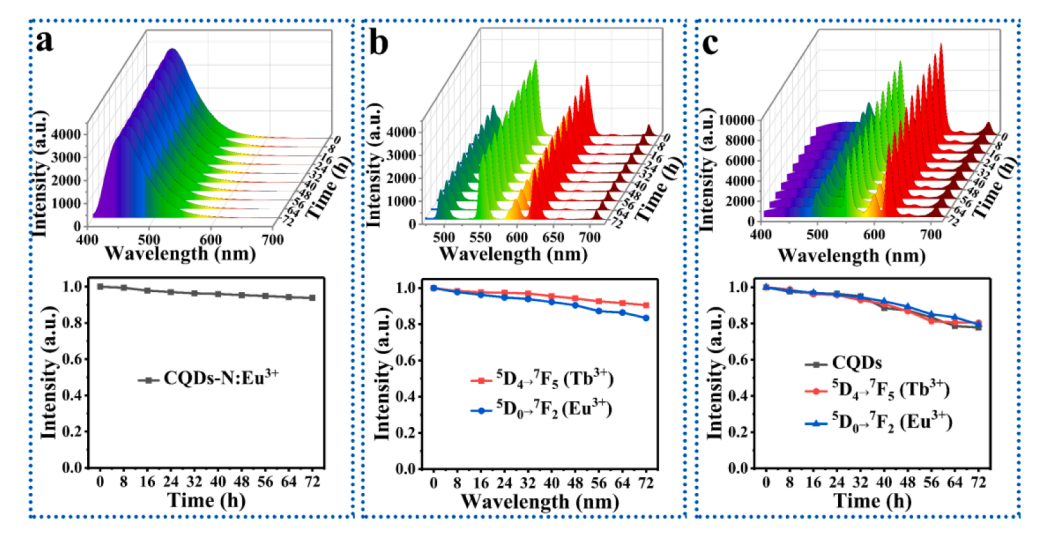


**Fig. 7.** Luminescence stability of samples. The time-dependent emission spectra under UV light and their corresponding integrated emission intensity as a function of time: (a) CQDs-N:5%Eu<sup>3+</sup>, (b) MOF-Gd:5%Eu<sup>3+</sup>/25%Tb<sup>3+</sup>, and (c) CNE-5@MOFG.

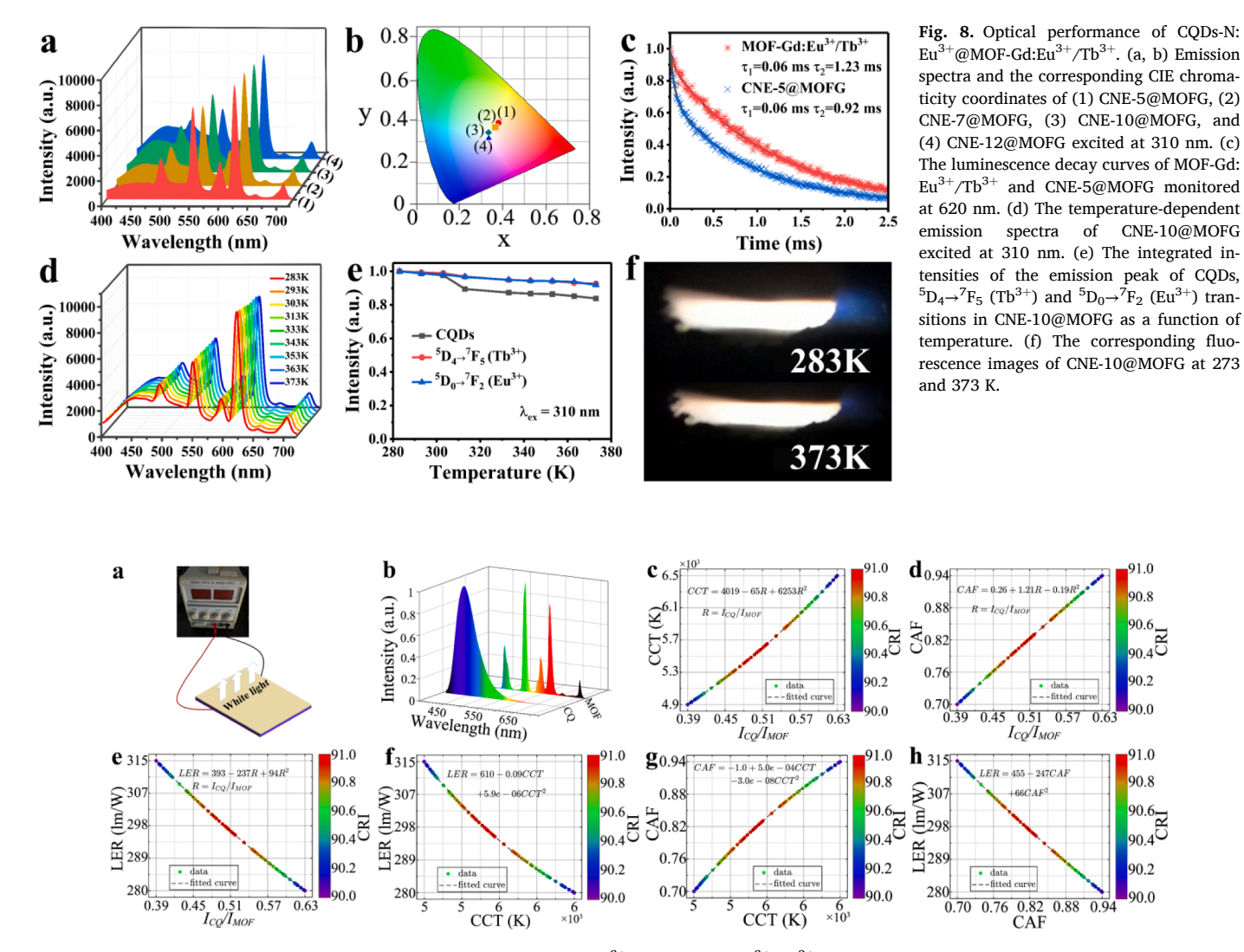
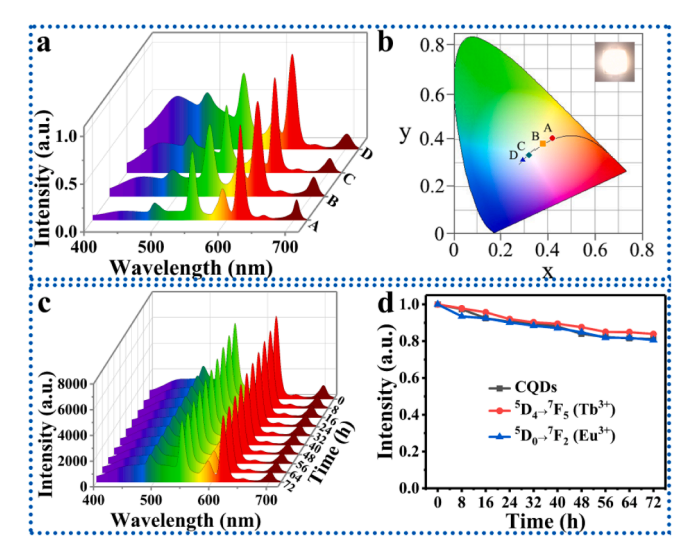


Fig. 9. Calculated the performance of WLEDs constructed with CQDs-N:Eu $^{3+}$  and MOF-Gd:Eu $^{3+}$ /Tb $^{3+}$ . (a) The schematic diagram of WLEDs device structure constructed with CQDs-N:Eu $^{3+}$  and MOF-Gd:Eu $^{3+}$ /Tb $^{3+}$  different materials. (b) The optimized emission spectra of CQDs-N:Eu $^{3+}$  and MOF-Gd:Eu $^{3+}$ /Tb $^{3+}$ . (c, d, e) CCT, LER, and CAF change with the emission ratio of CQDs-N:Eu $^{3+}$  to MOF-Gd:Eu $^{3+}$ /Tb $^{3+}$ . (f, g) LER and CAF change with the change of CCT. (h) LER changes with the change of CAF.



**Fig. 10.** The WLEDs devices constructed with CQDs-N:Eu $^{3+}$ @MOF-Gd:Eu $^{3+}$ /Tb $^{3+}$  single composite material. (a, b) Emission spectra and CIE chromaticity coordinates of phosphor-based WLEDs with different CCT (the inset is a photograph of WLED). (c, d) The time-dependent luminescence and the integrated emission intensity of LED-B as a function of time.

CTB  $\text{Ln}^{3+} \rightarrow \text{O}^{2-}$ , which can effectively transfer energy to both  $\text{Eu}^{3+}$  and  $\text{Tb}^{3+}$ .

By adjusting the Eu³+/Tb³+ molar ratios, four samples with different emission colors were obtained and the emission spectra are shown in Fig. 6a: (1) 5%Tb³+, (2) 5%Eu³+/25%Tb³+, (3) 5%Eu³+/5%Tb³+, (4) 5%Eu³+. It can be observed from the graph that the samples show characteristic peaks of Tb³+ at 491, 550, 594, and 620 nm, which are attributed to the  $^5\mathrm{D}_4\!\rightarrow^7\!F_J$  (J=6,5,4, and 3) transitions of Tb³+ ions, respectively. Similarly, the spectral peaks between 580 and 720 nm are assigned to the transitions of  $^5\mathrm{D}_0\!\rightarrow^7\!F_J$  (J=1,2,3, and 4) of Eu³+ ions. The corresponding values of  $\Omega_2$  are shown in Supplementary Table 9. The corresponding CIE chromaticity coordinates of MOF-Gd:Eu³+/Tb³+ are (0.313, 0.598), (0.439, 0.496), (0.514, 0.441) and (0.584, 0.323) for MOF-Gd:5%Tb³+, MOF-Gd:25%Tb³+/5%Eu³+, MOF-Gd:5%Tb³+/5%Eu³+, and MOF-Gd:5%Eu³+, respectively (Fig. 6b).

Next, we passivated the surface defects of CQDs by N, which greatly enhanced the luminous intensity of the CQDs (Fig. 6c and Supplementary Fig. 14). Then, the influence of the Eu<sup>3+</sup> concentration on the fluorescence properties of CQDs-N:Eu<sup>3+</sup> was studied. The corresponding emission spectra of the CQDs-N doped with different Eu<sup>3+</sup> concentrations are shown in Fig. 6c. The characteristic broad emission peaks at 450 nm of CQDs were obtained upon 380-nm excitation. The emission intensity of the doped CQDs-N as a function of Eu<sup>3+</sup> concentrations is shown in Supplementary Fig. 15a, which indicates the emission of the doped CQDs-N increased gradually with increasing Eu<sup>3+</sup> concentrations from 0 to 5 % and then decreased at higher  $\mathrm{Eu}^{3+}$  concentrations. The corresponding CIE chromaticity coordinates of CQDs-N:5%Eu<sup>3+</sup> were calculated to be (0.151, 0.085) (Supplementary Fig. 15b). Fig. 6d is the photograph of the four liquid samples dispersed under UV light irradiation. It can be seen from the photograph that we obtained the green, yellow, orange, red, and blue emissions independently.

To study the fluorescence stability of samples under UV irradiation, the time-dependent spectra of CQDs-N:5%Eu $^{3+}$ , MOF-Gd:5%Eu $^{3+}/25$ % Tb $^{3+}$ , and CNE-5@MOFG under UV light irradiation were recorded (Fig. 7). It can be seen from the graphs that decay rates of emission intensity are very slow, which proves that the CQDs-N:5%Eu $^{3+}$ , MOF-Gd:5%Eu $^{3+}/25$ %Tb $^{3+}$ , and CNE-5@MOFG have high stability under UV light irradiation.

To obtain the white light emission, we combined CQDs-N:Eu $^{3+}$  with blue light emission and MOF-Gd:Eu $^{3+}$ /Tb $^{3+}$  with yellow light emission to obtain CNE-x@MOFG (x = 5, 7, 10, and 12) composites.

Supplementary Fig. 16 shows the excitation and emission spectra of CNE-5@MOFG. The spectrum obtained by monitoring CNE-5@MOFG at 454 nm is composed of strong broadband at about 380 nm (Supplementary Fig. 16a). In addition, the excitation spectra of the emissions from Tb<sup>3+</sup> and Eu<sup>3+</sup> are shown in Supplementary Fig. 16(b,c), respectively. By monitoring the emission peaks of Tb<sup>3+</sup> at 549 nm and Eu<sup>3+</sup> at 621 nm, it can be observed that there are broad and strong excitation bands at 295 nm in the excitation spectra, which are mainly attributed to the absorption of MOF-Gd matrix and the CTB  $Ln^{3+} \rightarrow O^{2-}$ , and then the energy transferred to the excited energy levels of Tb<sup>3+</sup> and Eu<sup>3+</sup>, resulting in the strong emissions of Tb<sup>3+</sup> and Eu<sup>3+</sup> ions. In addition, it is observed that the broadbands of CQDs appeared at approximately 380 nm, indicating that CQDs transfer energy to Tb<sup>3+</sup> and Eu<sup>3+</sup>. The emission spectrum excited at 310 nm is also shown in Supplementary Fig. 16d. Excitation into the CODs band at 310 nm yields sharp and strong emissions at 492 nm and 549 nm, which are ascribed to the  $^5D_4 \rightarrow ^7F_6$  and  $^5D_4 \rightarrow ^7F_6$  transitions of Tb<sup>3+</sup> ions, respectively. As well as the sharp emissions between 580 nm and 720 nm are ascribed to the  $^{5}D_{0} \rightarrow ^{7}F_{I}(J=1, 2, 3, \text{ and 4})$  transitions of Eu<sup>3+</sup> ions. It is worth noting that the overlap between excitation and emission spectra of CNE-5@MOFG is quite small, which is conducive to increase the intensity of emission peaks.

Fig. 8a shows the emission spectra of CNE-x@MOFG (x = 5, 7, 10 and 12) excited at 310 nm. The corresponding values of  $\Omega_2$  are shown in Supplementary Table 10. As the amount of CQDs-N:Eu $^{3+}$  increases, the emission intensity of CQDs gradually increases and the correlated color temperature (CCT) gradually increases. This reveals that the CQDs-N: Eu $^{3+}$ @MOF-Gd:Eu $^{3+}$ /Tb $^{3+}$  samples can show the white light emissions with adjustable CCT under a single wavelength excitation. The corresponding CIE chromaticity coordinates of the CNE-x@MOFG (x = 5, 7, 10 and 12) samples were calculated to be (0.380, 0.389), (0.367, 0.368), (0.334, 0.343) and (0.334, 0.317), respectively (Fig. 8b). We also recorded the emission spectra of CNE-5@MOFG MOFG:xTb $^{3+}$  with different Tb $^{3+}$  concentrations (Supplementary Fig. 17). It can be seen from the graph that the emission intensity of Eu $^{3+}$  and Tb $^{3+}$  increases systematically with the increase of Tb $^{3+}$  concentration, which is consistent with the emission law of MOF-Gd:Eu $^{3+}$ /Tb $^{3+}$ .

To further study the possible luminescence mechanism of CQDs-N:  $Eu^{3+}@MOF\text{-}Gd:Eu^{3+}/Tb^{3+},\;\;we\;\;measured\;\;the\;\;luminescence\;\;decay\;\;curves\;of\; the\;\;^5D_0\rightarrow^7F_2\;\;transitions\;in\;\;MOF\text{-}Gd:Eu^{3+}/Tb^{3+}\;\;and\;\;CQDs\text{-}N: Eu^{3+}@MOF\text{-}Gd:Eu^{3+}/Tb^{3+}\;\;excited\;\;at\;310\;\;nm,\;\;respectively\;\;(Fig.\;8c).\;It\;\;can\;\;be\;\;seen\;\;from\;\;the\;\;figure\;\;that\;\;the\;\;fluorescence\;\;lifetimes\;of\;\;the\;\;CQDs-N:Eu^{3+}@MOF\text{-}Gd:Eu^{3+}/Tb^{3+}\;\;are\;\;much\;\;shorter\;\;than\;\;that\;\;of\;\;MOF\text{-}Gd:Eu^{3+}/Tb^{3+},\;which\;\;can\;\;be\;\;ascribed\;\;to\;\;the\;\;effective\;\;energy\;\;transfer\;\;from\;\;MOF\text{-}Gd:Eu^{3+}/Tb^{3+}\;\;to\;\;CQDs\text{-}N:Eu^{3+}.$ 

To study the thermal stability of samples, the temperature-dependent emission spectra of CNE-10@MOFG were recorded, as shown in Fig. 8d. Generally, the fluorescence intensity has a certain temperature dependence. The integrated intensities of the emission peak of CQDs,  ${}^5D_4 \rightarrow {}^7F_5$ (Tb<sup>3+</sup>) and  ${}^5D_0 \rightarrow {}^7F_2$  (Eu<sup>3+</sup>) transitions show a slight decrease with increasing temperature, which can be attributed to the thermal quenching effect and non-radiative trapping (Fig. 8e). Notably, the integrated emission intensity has a thermal quenching effect of less than 20 % with the temperature increase from 283 to 373 K, demonstrating the higher thermal stability and the smaller non-radiative recombination centers. The corresponding values of  $\Omega_2$  are shown in Supplementary Table 11, which indicating that the influence of temperature is relatively small. Fig. 8f shows the fluorescence images of CNE-10@MOFG at 273 K and 373 K, it can be seen from the images that the brightness of the sample hardly changes, indicating that the sample has high thermal stability.

#### 2.5. Applications in white LEDs.

We can not only construct WLEDs with CQDs-N: $Eu^{3+}$  and MOF-Gd:  $Eu^{3+}/Tb^{3+}$  materials, but also directly construct WLEDs with CQDs-N:

Eu<sup>3+</sup>@MOF-Gd:Eu<sup>3+</sup>/Tb<sup>3+</sup> single composite material. For the WLEDs constructed by CQDs-N:Eu<sup>3+</sup> and MOF-Gd:Eu<sup>3+</sup>/Tb<sup>3+</sup> materials, we systematically optimized the spectral of the designed composite structure according to the method reported in our previous work [48,49]. The WLEDs device structure and optimized spectra are shown in Fig. 9a,b, respectively. Supplementary Table 12 and Fig. 9c-h summarized and presented the optical properties obtained by extensive calculations and optimizations. For the white light with CRI higher than 90, the CCT (Fig. 9c) and CAF (Fig. 9d) can be increased by increasing the ratio of CQDs-N:Eu<sup>3+</sup> to MOF-Gd:Eu<sup>3+</sup>/Tb<sup>3+</sup> emission, while the LER (Fig. 9e) is the opposite. Therefore, we can increase the blue emission of CQDs-N: Eu<sup>3+</sup> to obtain cool white light (the higher CCT), and increase the hybrid color of MOF-Gd:Eu<sup>3+</sup>/Tb<sup>3+</sup> to obtain warm white light (the lower CCT). The higher the LER, the better the visual performance. As shown in Fig. 9f, the relationship between LER and CCT is nearly linear, and LER decreases as CCT increases. The influence of white light acquired by mixing different kinds of emissions on human health is represented in Fig. 9g. The CAF decreases by decreasing the CCT. In addition, a nearly linear relationship between CAF and LER was found. As shown in Fig. 9h, the trend is the same as the dependence of LER on CCT. Therefore, the white light obtained by the combination of CQDs-N:Eu<sup>3+</sup> and MOF-Gd:Eu<sup>3+</sup>/Tb<sup>3+</sup> has excellent color quality, good visual performance, and ideal CCT value. These findings provide reliable theoretical support for the application of this material in WLEDs. For the WLEDs devices constructed with CQDs-N:Eu<sup>3+</sup>@MOF-Gd:Eu<sup>3+</sup>/Tb<sup>3+</sup> single composite material. The strong multi-color visible light emission of the obtained CQDs-N:Eu<sup>3+</sup>@MOF-Gd:Eu<sup>3+</sup>/Tb<sup>3+</sup> under singlewavelength excitation prompted us to develop their application in light-emitting diodes to develop next-generation display technologies.

As mentioned above, we fabricated WLEDs with adjustable CCT by depositing CQDs-N:Eu³+@MOF-Gd:Eu³+/Tb³+ composite materials on 310-nm near-UV light-emitting diode chips. Fig. 10a shows the mission spectra of four LEDs and Fig. 10b is the corresponding color coordinate diagram. We manufactured a warm white LED with high CRI by adjusting the ratio of CQDs-N:Eu³+ and MOF-Gd:Eu³+/Tb³+ (LED-B in Supplementary Table 13). The corresponding CCT is 4035 K, and CRI is as high as 95. The illustration in Fig. 10b shows a photograph of the operating LED-B. Therefore, the use of LEDs based on CQDs-N: Eu³+@MOF-Gd:Eu³+/Tb³+ light-emitting materials have good color quality and remarkable visual performance.

In addition, the LEDs with adjustable color temperature from warm white to cool white (LED-A, LED-C, and LED-D in Supplementary Table 13) were manufactured, and the corresponding CCT values were 3283 K, 6041 K, and 7861 K. Among them, the CIE value of LED-C is (0.32, 0.33), which is practically identical to the standard white light CIE value specified by NTSC (National Television Systems Committee). The pure white light CIE chromaticity coordinates specified by NTSC is (0.33, 0.33). The color characteristics of these four LEDs were shown in Supplementary Table 13. The time-dependent luminescence spectra of LED-B were used to study the stability of WLEDs. Fig. 10c shows the time-dependent spectra, and Fig. 10d is the corresponding integrated emission intensity. It can be observed from the graphs that the decay rates of light intensity of the emission peak of CQDs,  ${}^5D_4 \rightarrow {}^7F_5$  and  $^5D_0 \rightarrow ^7F_2$  transitions are slower in 72 h, which proves the WLED has high stability. The WLEDs based on CQDs-N:Eu<sup>3+</sup>@MOF-Gd:Eu<sup>3+</sup>/Tb<sup>3+</sup> has good visual performance, ideal CCT and CAF, and high LER, which further proves their great potential applications in the development of lighting and next-generation display technology.

In addition, we also obtained almost multicolor (green, red, and yellow) phosphor LEDs devices with good performance, as shown in Supplementary Fig. 18. The CIE chromaticity coordinates of emission spectra are (0.338, 0.573), (0.543, 0.309) and (0.418, 0.432), respectively.

#### 3. Conclusion

In this work, the white light-emitting CQDs-N:Eu<sup>3+</sup>@MOF-Gd:Eu<sup>3+</sup>/ Tb<sup>3+</sup> composite materials based on lanthanide single atom were prepared by the simple and low-cost hydrothermal method, which have the structural advantages of MOF-Ln host and the light-emitting advantages of doped CQDs-N guest and MOF-Ln host. The DFT was used to optimize the structures of the CQDs-N:Eu<sup>3+</sup> and MOF-Ln (Ln = Gd, Eu, and Tb), which show that C atoms are more favorable for anchoring Eu<sup>3+</sup> single atoms rather than being doped or replaced. In addition, the work function, optical properties, and charge differential density were also calculated. Significantly, this composite material exhibited the characteristic emissions of CQDs (454 nm), Tb<sup>3+</sup> (492 and 549 nm), and Eu<sup>3+</sup> (594, 621, 656, and 705 nm) under the 310 nm near-ultraviolet (UV) light excitation, and obtained white light emission with adjustable color temperature by adjusting the ratios of CQDs-N:Eu<sup>3+</sup> and MOF-Gd: Eu<sup>3+</sup>/ Tb<sup>3+</sup> in the single phosphor. The WLED devices not only can be constructed by using CQDs-N:Eu<sup>3+</sup> and MOF-Gd:Eu<sup>3+</sup>/Tb<sup>3+</sup> materials, but also can be constructed by using the CODs-N:Eu<sup>3+</sup>@MOF-Gd:Eu<sup>3+</sup>/Tb<sup>3+</sup> single composite material. Moreover, the UV-pumped single CQDs-N: Eu<sup>3+</sup>@MOF-Gd:Eu<sup>3+</sup>/Tb<sup>3+</sup> phosphor-based warm WLED devices with a high CRI of 95 and an ideal CCT of 4035 K were obtained. Overall, this work opens up a new way to explore low-cost, high-performance WLEDs.

#### **Declaration of Competing Interest**

The authors declare that they have no known competing financial interests or personal relationships that could have appeared to influence the work reported in this paper.

#### Acknowledgments

This work was supported by the National Natural Science Foundation of China (No. 21871079 and 11774128), the Natural Science Foundation of Shandong Province (ZR2018JL003, 2019KJJ003), and the National Science Foundation (No. 1945558).

#### Appendix A. Supplementary data

Supplementary data to this article can be found online at https://doi.org/10.1016/j.cej.2021.132782.

#### References

- [1] L. Wang, X. Wang, F. Bertram, B.W. Sheng, Z.B. Hao, Y. Luo, C.Z. Sun, B. Xiong, Y. J. Han, J. Wang, H.T. Li, G. Schmidt, P. Veit, J. Christen, X.Q. Wang, Color-tunable 3D InGaN/GaN multi-quantum-well light-emitting-diode based on microfacet emission and programmable driving power supply, Adv. Opt. Mater. 9 (2021) 9.
- [2] J.W. Qiao, G.J. Zhou, Y.Y. Zhou, Q.Y. Zhang, Z.G. Xia, Divalent europium-doped near-infrared-emitting phosphor for light-emitting diodes, Nat. Commun. 10 (2019) 5267.
- [3] G.F. Wang, Q. Peng, Y.D. Li, Lanthanide-doped nanocrystals: synthesis, optical-magnetic properties, and applications, Acc. Chem. Res. 44 (2011) 322–332.
- [4] Y.S. Xu, Z.C. Zeng, D. Zhang, S.T. Liu, X. Wang, S. Li, C.Y. Cheng, J.X. Wang, Y. Liu, G.J.H. De, C. Zhang, W.P. Qin, Y.P. Du, Upconversion lifetime imaging of highly-crystalline gd-based fluoride nanocrystals featuring strong luminescence resulting from multiple luminescent centers, Adv. Opt. Mater. 8 (2020) 9.
- [5] J. Qiao, L. Ning, M.S. Molokeev, Y.-C. Chuang, Q. Liu, Z. Xia, Eu<sup>2+</sup> site preferences in the mixed cation K<sub>2</sub>BaCa(PO<sub>4</sub>)<sub>2</sub> and thermally stable luminescence, J. Am. Chem. Soc. 140 (30) (2018) 9730–9736.
- [6] L. Wang, R.J. Xie, T. Suehiro, T. Takeda, N. Hirosaki, Down-conversion nitride materials for solid state lighting: recent advances and perspectives, Chem. Rev. 118 (2018) 1951–2009.
- [7] H. Zhang, Q. Su, S.M. Chen, Quantum-dot and organic hybrid tandem lightemitting diodes with multi-functionality of full-color-tunability and white-lightemission. Nat. Commun. 11 (2020) 8.
- [8] C. Sun, Y.U. Zhang, C. Ruan, C. Yin, X. Wang, Y. Wang, W.W. Yu, Efficient and stable white leds with silica-coated inorganic perovskite quantum dots, Adv. Mater. 28 (45) (2016) 10088–10094.

- [9] M. Pan, W.-M. Liao, S.-Y. Yin, S.-S. Sun, C.-Y. Su, Single-phase white-light-emitting and photoluminescent color tuning coordination assemblies, Chem. Rev. 118 (18) (2018) 8889–8935.
- [10] T. Feng, Q. Zeng, S. Lu, X. Yan, J. Liu, S. Tao, M. Yang, B. Yang, Color-tunable carbon dots possessing solid-state emission for full color light-emitting diodes applications, ACS Photonics 5 (2) (2018) 502–510.
- [11] J. Xu, X.Y. Chen, Y.S. Xu, Y.P. Du, C.H. Yan, Ultrathin 2D rare-earth nanomaterials: compositions, syntheses, and applications, Adv. Mater. 32 (2020) 17.
- [12] N. Phung, R. Félix, D. Meggiolaro, A. Al-Ashouri, G. Sousa e Silva, C. Hartmann, J. Hidalgo, H. Köbler, E. Mosconi, B. Lai, R. Gunder, M. Li, K.-L. Wang, Z.-K. Wang, K. Nie, E. Handick, R.G. Wilks, J.A. Marquez, B. Rech, T. Unold, J.-P. Correa-Baena, S. Albrecht, F. De Angelis, M. Bär, A. Abate, The doping mechanism of halide perovskite unveiled by alkaline earth metals, J. Am. Chem. Soc. 142 (5) (2020) 2364–2374.
- [13] T. Fleetham, G.J. Li, J. Li, Phosphorescent Pt(II) and Pd(II) complexes for efficient, high-color-quality, and stable OLEDs, Adv. Mater. 29 (2017) 16.
- [14] L.T. Zhang, W.M. Kang, Q. Ma, Y.F. Xie, Y.L. Jia, N.P. Deng, Y.Z. Zhang, J. Ju, B. W. Cheng, Two-dimensional acetate-based light lanthanide fluoride nanomaterials (F-Ln, Ln = La, Ce, Pr, and Nd): morphology, structure, growth mechanism, and stability, J. Am. Chem. Soc. 141 (2019) 13134–13142.
- [15] H.Y. Xu, W.J. Yu, K. Pan, G.F. Wang, P.F. Zhu, Confinement and antenna effect for ultrasmall y<sub>2</sub>0<sub>3</sub>:eu<sup>3+</sup> nanocrystals supported by mof with enhanced near-uv light absorption thereby enhanced luminescence and excellently multifunctional applications, Nano Res. 14 (2021) 720–729.
- [16] X.Y. Huang, Full-color persistent luminescence tuning: a marriage of perovskite quantum dots and lanthanide ions, Sci. China-Mater. 63 (2020) 165–166.
- [17] B. Yan, Lanthanide-functionalized metal-organic framework hybrid systems to create multiple luminescent centers for chemical sensing, Acc. Chem. Res. 50 (11) (2017) 2789–2798.
- [18] A. Karmakar, P. Samanta, A.V. Desai, S.K. Ghosh, Guest-responsive metal-organic frameworks as scaffolds for separation and sensing applications, Acc. Chem. Res. 50 (10) (2017) 2457–2469.
- [19] Z. Cui, X.Y. Zhang, S. Liu, L. Zhou, W.L. Li, J.P. Zhang, Anionic lanthanide metalorganic frameworks: selective separation of cationic dyes, solvatochromic behavior, and luminescent sensing of Co(II) Ion, Inorg. Chem. 57 (2018) 11463–11473.
- [20] M. Pan, Y.-X. Zhu, K. Wu, L. Chen, Y.-J. Hou, S.-Y. Yin, H.-P. Wang, Y.-N. Fan, C.-Y. Su, Epitaxial growth of hetero-In-mof hierarchical single crystals for domain-and orientation-controlled multicolor luminescence 3d coding capability, Angew. Chem. Int. Edit. 56 (46) (2017) 14582–14586.
- [21] M.L. Gao, W.J. Wang, L. Liu, Z.B. Han, N. Wei, X.M. Cao, D.Q. Yuan, Microporous hexanuclear In(iii) cluster-based metal-organic frameworks: color tunability for barcode application and selective removal of methylene blue, Inorg. Chem. 56 (2017) 511–517.
- [22] X. Yang, X. Lin, Y. Zhao, Y.S. Zhao, D. Yan, Lanthanide metal-organic framework microrods: colored optical waveguides and chiral polarized emission, Angew. Chem. Int. Edit. 56 (27) (2017) 7853–7857.
- [23] Y.-W. Zhao, F.-Q. Zhang, X.-M. Zhang, Single component lanthanide hybrids based on metal-organic framework for near-ultraviolet white light LED, ACS Appl. Mater. Interfaces 8 (36) (2016) 24123–24130.
- [24] D.Y. Xia, P. Wang, X.F. Ji, N.M. Khashab, J.L. Sessler, F.H. Huang, Functional supramolecular polymeric networks: the marriage of covalent polymers and macrocycle-based host-guest interactions, Chem. Rev. 120 (2020) 6070–6123.
- [25] D.S. Zhang, Q. Gao, Z. Chang, X.T. Liu, B. Zhao, Z.H. Xuan, T.L. Hu, Y.H. Zhang, D. Zhu, X.H. Bu, Rational construction of highly tunable donor-acceptor materials based on a crystalline host-guest platform, Adv. Mater. 30 (2018) 7.
- [26] F. Hong, H.P. Xu, G. Pang, G.X. Liu, X.T. Dong, W.S. Yu, Moisture resistance, luminescence enhancement, energy transfer and tunable color of novel core-shell structure BaGeF<sub>6</sub>:Mn<sup>4+</sup> phosphor, Chem. Eng. J. 390 (2020) 12.
   [27] M.K. Albolkany, Y. Wang, W.J. Li, S. Arooj, C.H. Chen, N.N. Wu, Y. Wang,
- [27] M.K. Albolkany, Y. Wang, W.J. Li, S. Arooj, C.H. Chen, N.N. Wu, Y. Wang, R. Zboril, R.A. Fischer, B. Liu, Dual-function HKUST-1: templating and catalyzing formation of graphitic carbon nitride quantum dots under mild conditions, Angew. Chem. Int. Edit. 59 (2020) 21499–21504.
- [28] Y. Wen, T. Sheng, X. Zhu, C. Zhuo, S. Su, H. Li, S. Hu, Q.-L. Zhu, X. Wu, Introduction of red-green-blue fluorescent dyes into a metal-organic framework for tunable white light emission, Adv. Mater. 29 (2017) 1700778.
- [29] Ü. Kökçam-Demir, A. Goldman, L. Esrafili, M. Gharib, A. Morsali, O. Weingart, C. Janiak, Coordinatively unsaturated metal sites (open metal sites) in metal-

- organic frameworks: design and applications, Chem. Soc. Rev. 49 (9) (2020) 2751–2798.
- [30] Z.F. Wang, F.L. Yuan, X.H. Li, Y.C. Li, H.Z. Zhong, L.Z. Fan, S.H. Yang, 53% Efficient red emissive carbon quantum dots for high color rendering and stable warm white-light-emitting diodes, Adv. Mater. 29 (2017) 7.
- [31] H. Ding, S.-B. Yu, J.-S. Wei, H.-M. Xiong, Full-color light-emitting carbon dots with a surface-state-controlled luminescence mechanism, ACS Nano 10 (1) (2016) 484–491.
- [32] C.L. Xia, S.J. Zhu, T.L. Feng, M.X. Yang, B. Yang, Evolution and synthesis of carbon dots: from carbon dots to carbonized polymer dots, Adv. Sci. 6 (2019) 1901316.
- [33] H. Ding, J.S. Wei, P. Zhang, Z.Y. Zhou, Q.Y. Gao, H.M. Xiong, Solvent-controlled synthesis of highly luminescent carbon dots with a wide color gamut and narrowed emission peak widths, Small 14 (2018) 10.
- [34] S. Bhattacharya, R.S. Phatake, S.N. Barnea, N. Zerby, J.J. Zhu, R. Shikler, N. G. Lemcoff, R. Jelinek, Fluorescent self-healing carbon dot/polymer gels, ACS Nano 13 (2019) 1433–1442.
- [35] Y. Pang, J.S. Wei, Y.G. Wang, Y.Y. Xia, Synergetic protective effect of the ultralight mwcnts/ncqds modified separator for highly stable lithium-sulfur batteries, Adv. Energy. Mater. 8 (2018) 1702288.
- [36] Y. Liu, X. Li, Q. Zhang, W. Li, Y.U. Xie, H. Liu, L.u. Shang, Z. Liu, Z. Chen, L. Gu, Z. Tang, T. Zhang, S. Lu, A general route to prepare low-ruthenium-content bimetallic electrocatalysts for ph-universal hydrogen evolution reaction by using carbon quantum dots, Angew. Chem. Int. Edit. 59 (4) (2020) 1718–1726.
- [37] F. Arcudi, L. Dordević, M. Prato, Synthesis, separation, and characterization of small and highly fluorescent nitrogen-doped carbon nanodots, Angew. Chem. Int. Edit. 55 (6) (2016) 2107–2112.
- [38] P. Long, Y.Y. Feng, C. Cao, Y. Li, J.K. Han, S.W. Li, C. Peng, Z.Y. Li, W. Feng, Self-protective room-temperature phosphorescence of fluorine and nitrogen codoped carbon dots, Adv. Funct. Mater. 28 (2018) 1800791.
- [39] K. Holá, M. Sudolská, S. Kalytchuk, D. Nachtigallová, A.L. Rogach, M. Otyepka, R. Zbořil, Graphitic nitrogen triggers red fluorescence in carbon dots, ACS Nano 11 (12) (2017) 12402–12410.
- [40] R.S. Li, J.H. Liu, T. Yang, P.F. Gao, J. Wang, H. Liu, S.J. Zhen, Y.F. Li, C.Z. Huang, Carbon quantum dots-europium(iii) energy transfer architecture embedded in electrospun nanofibrous membranes for fingerprint security and document counterspy, Anal. Chem. 91 (17) (2019) 11185–11191.
- [41] C. Gao, J.X. Low, R. Long, T.T. Kong, J.F. Zhu, Y.J. Xiong, Heterogeneous singleatom photocatalysts: fundamentals and applications, Chem. Rev. 120 (2020) 12175–12216.
- [42] Q.I. Wang, X. Huang, Z.L. Zhao, M. Wang, B. Xiang, J. Li, Z. Feng, H.U. Xu, M. Gu, Ultrahigh-loading of ir single atoms on nio matrix to dramatically enhance oxygen evolution reaction, J. Am. Chem. Soc. 142 (16) (2020) 7425–7433.
- [43] Y.U. Xiong, J. Dong, Z.-Q. Huang, P. Xin, W. Chen, Y.U. Wang, Z. Li, Z. Jin, W. Xing, Z. Zhuang, J. Ye, X. Wei, R. Cao, L. Gu, S. Sun, L. Zhuang, X. Chen, H. Yang, C. Chen, Q. Peng, C.-R. Chang, D. Wang, Y. Li, Single-atom Rh/N-doped carbon electrocatalyst for formic acid oxidation, Nat. Nanotechnol. 15 (5) (2020) 390–397.
- [44] J. Fu, J. Dong, R. Si, K. Sun, J. Zhang, M. Li, N. Yu, B. Zhang, M.G. Humphrey, Q. Fu, J. Huang, Synergistic effects for enhanced catalysis in a dual single-atom catalyst, Acs Catalysis 11 (4) (2021) 1952–1961.
- [45] Y.U. Xiong, W. Sun, Y. Han, P. Xin, X. Zheng, W. Yan, J. Dong, J. Zhang, D. Wang, Y. Li, Cobalt Single Atom Site Catalysts with Ultrahigh Metal Loading for Enhanced Aerobic Oxidation of Ethylbenzene, Nano Res. 6. 14 (7) (2021) 2418–2423.
- [46] S. Ji, Y. Qu, T. Wang, Y. Chen, G. Wang, X. Li, J. Dong, Q.Y. Chen, W. Zhang, Z. Zhang, S. Liang, R. Yu, Y.U. Wang, D. Wang, Y. Li, Rare-earth single erbium atoms for enhanced photocatalytic CO<sub>2</sub> reduction, Angew. Chem. Int. Edit. 59 (26) (2020) 10651–10657.
- [47] L. Xu, Y. Li, Q. Pan, D. Wang, S. Li, G. Wang, Y. Chen, P. Zhu, W. Qin, Dual-mode light-emitting lanthanide metal-organic frameworks with high water and thermal stability and their application in white LEDs, ACS Appl. Mater. Interfaces 12 (16) (2020) 18934–18943.
- [48] P. Zhu, H. Zhu, G.C. Adhikari, S. Thapa, Spectral optimization of white light from hybrid metal halide perovskites, Osa Continuum. 2 (6) (2019) 1880, https://doi. org/10.1364/OSAC.2.001880.
- [49] P. Zhu, H. Zhu, G.C. Adhikari, S. Thapa, Design of circadian white light-emitting diodes with tunable color temperature and nearly perfect color rendition, Osa Continuum. 2 (8) (2019) 2413, https://doi.org/10.1364/OSAC.2.002413.